Using Atomically-thin Hexagonal Boron Nitride Layer to Separate Bound Charge Transfer Excitons at Organic Interfaces

Shanika Wanigasekara[1], Kushal Rijal[1], Fatimah Rudayni[1,2], Mohan Panth[1], Andrew Shultz[1], Judy Z. Wu[1], Wai-Lun Chan[1, *]

1. Department of Physics and Astronomy, University of Kansas, Lawrence, Kansas 66045, US
2. Department of Physics, Jazan University, Jazan 45142, Saudi Arabia

Abstract

We successfully use two-dimensional hexagonal boron nitride (h-BN) as a continuous and ultrathin insulator to facilitate the conversion of excitons into free carriers at organic donor-acceptor (D-A) interfaces. A monolayer (0.33 nm) thick h-BN with a lateral size on the order of 1 cm^2 was inserted between zinc phthalocyanine (ZnPc) and perylenetetracarboxylic diimide (PTCDI) organic films that form a generic D-A interface. We found that the h-BN increases the photon-to-free carrier conversion yield of the D-A heterostructure by 130% as compared to identical samples without an h-BN layer, even though the h-BN lowers the initial electron transfer rate from ZnPc to PTCDI. The enhanced photon-to-free carrier conversion yield is attributed to a larger charge separation yield of charge transfer (CT) excitons at the D-A interface. The h-BN can prohibit the formation of tightly bound CT excitons and impede electron-hole recombination, which can improve the charge separation yield.

*wlchan@ku.edu

I. INTRODUCTION

Exciton dissociation is a critical process for converting photons into free carriers in organic photovoltaic (OPV) and optoelectronic devices. At a typical organic donor-accepter (D-A) interface, the electron and hole, separated by the D-A interface, remain bound together by their Columbic interaction. This bound electron-hole pair is known as a charge transfer (CT) exciton [1-5]. The binding energy of the CT exciton increases with the decrease in the electron-hole separation, and it can reach as large as ~0.5 eV when electron and hole are localized next to each other at the D-A interface [6,7]. Thermodynamically, these tightly bound CT excitons mostly recombine unless an E-field is present near the interface to assist the separation of the CT exciton and to sweep out the separated charges. Hence, a large energy loss is often required to achieve a high charge separation (CS) yield. This energy loss has been identified as a major factor that limits the open circuit voltage and the OPV efficiency [8-10]. One of the strategies to increase the CS yield is to avoid the formation of these tightly bound CT excitons. This can be achieved, for instance, by inserting a molecularly thin insulating layer at the D-A interface, which spatially separates donor and acceptor molecules, and hence lowers the CT exciton binding energy. The insulating layer can further improve the CS yield by suppressing both geminate and non-geminate recombination.

However, implementing this strategy with traditional thin film materials can be very challenging. Previously, wide-band gap organic molecules [11] or ionic compounds such as LiF [12] were used. These materials unavoidably mix with donor or acceptor molecules at the D-A interface physically *via* diffusion. The interlayer mixing makes the thin insulating barrier spatially non-uniform, on which bound CT excitons can still form readily at some porous areas. In order to form a continuous and effective insulating barrier, a thicker insulating layer is often needed. However, a thicker interlayer significantly impedes the CT between donor and acceptor molecules. When the interfacial CT process is impeded, the CT exciton cannot be

formed in the first place. Because of this trade off, there has been limited success in using this strategy to improve the CS yield. Even for some successful demonstrations, the insulating layer can only incrementally improve the OPV efficiency within a very narrow window of the insulating layer thickness (~ 0.5 - 1 nm) [11]. In addition, the non-ideal interlayer can lower the efficiency as compared to similar devices without the insulating layer when its thickness is either below or above the optimal range.

Compared to traditional thin film materials, two dimensional (2D) van der Waals (vdW) materials provide a more viable pathway to control the interfacial structure at the atomic scale. Moreover, the natural compatibility between 2D crystals and organic molecules (both are vdW materials) results in recent research interests on designing organic-2D hybrid heterostructures for various applications [13-16]. With the maturing of the growth and transfer techniques of 2D layered crystals, inserting atomically thin yet continuous insulating layer between the donor and acceptor layers becomes feasible. For example, we have recently developed a dry transfer method for transferring cm-sized, continuously graphene onto organic films without immersing the organic layer into any solvents [17]. This scalable method can, in principle, be used to transfer other 2D crystals as well. In this work, we used this method to transfer monolayer (ML) hexagonal boron nitride (h-BN) onto an organic thin film. A ML h-BN is one of the thinnest (0.33 nm) yet continuous insulating materials (bandgap ~ 6 eV) that one can fabricate [18]. A continuous, ultrathin insulator minimizes its adverse impacts on the CT process, while effectively weakens the CT exciton binding and reduces the electron-hole recombination rate.

In this work, we have successfully produced a cm-sized donor/h-BN/acceptor multilayer structure. Comparing the samples with and without the h-BN interlayer, we found that although the ML h-BN reduces the initial CT rate at the D-A interface, it increases the ns-transient photon-to-free carrier conversion yield by ~ 130 % under an open circuit condition. In other words, the conversion yield is more than doubled after the h-BN is inserted to the D-

A interface. The increase in the photon-to-free carrier conversion yield demonstrates that the h-BN interlayer effectively assists the CS process by prohibiting the formation of tightly-bound CT excitons and reducing the CT exciton recombination. It can potentially be incorporated into various planar heterostructures [19,20]. Finally, ML h-BN is mechanically flexible and optically transparent. Therefore, it is highly suitable to be used in ultrathin, flexible, or semi-transparent organic devices.

II. EXPERIMENTAL METHODS

Organic thin film deposition: The model D-A interface used in this work consists of N,N′-dimethyl perylenetetracarboxylic diimide (PTCDI) as the acceptor and zinc phthalocyanine (ZnPc) as the donor. The PTCDI (Luminescence Technology, >99%) was deposited on a graphene-on-SiO_2/Si substrate using thermal evaporation in an ultrahigh vacuum (UHV) chamber with a base pressure of 10^{-9} Torr. For some samples, the ML h-BN was transferred on top of the PTCDI film (see the dry transfer procedure below). Then, ZnPc (Luminescence Technology, >99%) was deposited on top of the as-prepared sample. The deposition rates were kept at 0.3-0.4 Å/min and 0.8-1.0 Å/min for PTCDI and ZnPc, respectively. The thickness of the organic film was monitored using a quartz crystal microbalance.

Dry transfer for ML h-BN: CVD-grown, ML h-BN on Cu (purchased from Graphene Supermarket) was used. A polyethylene terephthalate (PET)/silicone stamp was employed to transfer the h-BN onto the PTCDI film. Similar methods have been used to transfer ML graphene [17,21]. First, a 1 cm × 0.5 cm h-BN/Cu was pressed onto the PET/silicone stamp by applying a mild pressure for 1 hour. The PET/silicone/h-BN/Cu stack was then stored in a high vacuum (HV) chamber overnight (base pressure ~ 10^{-7} Torr) to improve the adhesion. Next, the Cu foil was etched away using Cu etchant solution ($FeCl_3$). Similar to the PMMA-assisted wet transfer method [22], the h-BN sample was rinsed/washed repeatedly with hydrochloric

acid, ammonium hydroxide solution, and deionized water to remove any contaminants. After these cleaning steps, the PET/silicone/h-BN stack was dried with N_2 gas and stored in the HV chamber before used. During the final transfer process, both the PTCDI and the PET/silicone/h-BN were taken out from the vacuum for a few minutes, and the PET/silicone/h-BN stack was pressed onto the PTCDI surface in ambient environment. Then, the whole sample was stored inside the HV chamber overnight, which improved the adhesion between the h-BN and the organic film. The whole sample was then taken out from the HV chamber for around one minute to remove the PET/silicone stamp. After the dry transfer, the sample was loaded immediately back into the vacuum system. Before depositing the ZnPc layer, the sample was outgassed inside the UHV deposition chamber at 90 °C overnight.

Time-resolved two-photon photoemission spectroscopy (TR-TPPE): The ultrafast CT rate from ZnPc (donor) to PTCDI (acceptor) was measured by TR-TPPE. In the TR-TPPE measurement, 25 fs pump laser pulses with a photon energy of 1.77 eV, which is smaller than the optical bandgap of PTCDI, was used to selectively excite the singlet (S_1) exciton of the ZnPc. The transient population of the ZnPc's S_1 exciton was probed by time-delayed 60 fs probe laser pulses with a photon energy of 4.68 eV. The probe pulse ionized the electron of the S_1 exciton. The spectrum (intensity vs the electron kinetic energy) for the emitted electrons was measured by a hemispherical electron analyzer (SPECS, Phoibos 100). Pump and probe pulses were generated from two non-collinear optical parametric amplifiers (NOPA, Orpheus-N-2H; Orpheus-N-3H, Light Conversion). Both NOPAs were pumped by a Yb:KGW regenerative amplifier running at 125 kHz (Pharos 10W, Light Conversion). The beam size had a full-width half-maximum (fwhm) of 0.8 mm at the sample. During the measurement, the sample was kept in an UHV chamber with a base pressure of 1×10^{-10} Torr.

Time-resolved graphene field effect transistor (TR-GFET) measurements: The amount of free charges generated by the CS process were measured optoelectronically by using

a GFET charge sensor [23,24]. The multilayer sample, either ZnPc/PTCDI or ZnPc/h-BN/PTCDI, was fabricated on top of a 1 mm × 1 mm graphene channel. The source and drain electrodes and the graphene channel were pre-patterned using shadow masks. During the measurement, the sample was kept in an optical cryostat (base pressure ~ 10^{-6} Torr). The sample was excited by 25-fs laser pulses generated by a NOPA (Light Conversion, Orpheus-N-2H). The laser wavelength was set at 700 nm. The laser repetition rate was reduced to 100 Hz by a built-in pulse picker to ensure that all separated charges produced by a laser pulse have recombined prior to the arrival of the next laser pulse. The pulse energy was ~ 340 nJ with a fwhm size of ~ 1.2 mm. The laser beam size was much larger than the grain size of our organic films, which is on the order of 1-10 μm.[25] Hence, our measurement probed the average property of the whole film and was not affected by the local variation in the film thickness originated from the surface/interface roughness. At 700 nm, photons were primarily absorbed by the topmost ZnPc layer. A portion of separated electrons generated by the CS process, which survived recombination events, can transfer to the graphene. The charge injection in turn induced a conductivity change in the graphene channel. The conductivity change as a function of time was captured by a 200 MHz oscilloscope (Keysight DSOX2024A). In some measurements, a voltage was applied to the Si back gate of the GFET sensor for quantifying the amount of free carriers generated from the CS process. For time-resolved measurements, the graphene was transferred onto a glass substrate (without the back gate) instead of a SiO_2(300 nm)/Si substrate in order to obtain a better time resolution [23].

III. RESULTS AND DISSCUSSION

A number of experimental techniques were used to characterize ZnPc/h-BN/PTCDI and ZnPc/PTCDI heterostructures. The result section will be organized as follow. First, we will show results obtained from Raman spectroscopy and ultraviolet photoemission spectroscopy (UPS). These results demonstrate that a continuous layer of h-BN can be transferred onto the

PTCDI, and the presence of the h-BN does not significantly change the HOMO level alignment between the ZnPc and PTCDI layers. Second, we will discuss the CT dynamics measured by the TR-TPPE. It is found that the h-BN increases the interfacial CT time from 190 fs to 270 fs. Despite of a slower CT time, CT excitons can still form across the D-A interface. The overall photon-to-free carrier conversion yield depends on the CS yield of these CT excitons. In the third part of this section, we will show results from the TR-GFET experiment, which probes the overall photon-to-free carrier conversion yield. It is found that the h-BN increases the conversion yield by 130 %.

A. Characterization of the ZnPc/h-BN/PTCDI multilayer structure

Samples consisting of PTCDI, ML h-BN and ZnPc were fabricated on graphene unless otherwise stated. Figure 1a shows a schematic diagram of the layered structure used in this work. The ML-h-BN was transferred on the PTCDI layer using a dry transfer method that we have developed for transferring graphene [17]. An optical microscope image near the edge of the h-BN is shown in Fig. 1b where a continuous h-BN layer can be observed.

To further demonstrate the ML h-BN on PTCDI is continuous, the transferred h-BN was probed by Raman spectroscopy. Raman spectra were taken with a commercial Raman imaging system (WiTec alpha300) equipped with a 532 nm laser. To avoid the confusion of the h-BN peak with the graphene D-peak, the sample used for the Raman spectroscopy does not contain the underlying graphene layer. Figure 1c shows a pair of Raman spectra taken from the 3-nm ZnPc/h-BN/5-nm PTCDI/SiO_2/Si (red) and 3-nm ZnPc/5-nm PTCDI/SiO_2/Si (blue) samples. For the sample with the h-BN, an additional peak at 1362 cm^{-1} is observed (labeled by a star in Fig. 1c), which can be attributed to the B-N vibrational mode (E_{2g}) of the h-BN layer [26]. Other peaks in the spectra can be assigned to the two molecules because all these peaks can be found in samples with and without h-BN. Note that the E_{2g} peak is located at ~ 1370 cm^{-1} when the ML h-BN is transferred on the SiO_2/Si substrate (Fig. 1d). The slight shift

in the Raman peak position would be originated from the interaction between the h-BN and the molecules. Figure 1e shows the Raman mapping image for the h-BN E_{2g} peak. The uniform intensity map indicates that the h-BN is continuous.

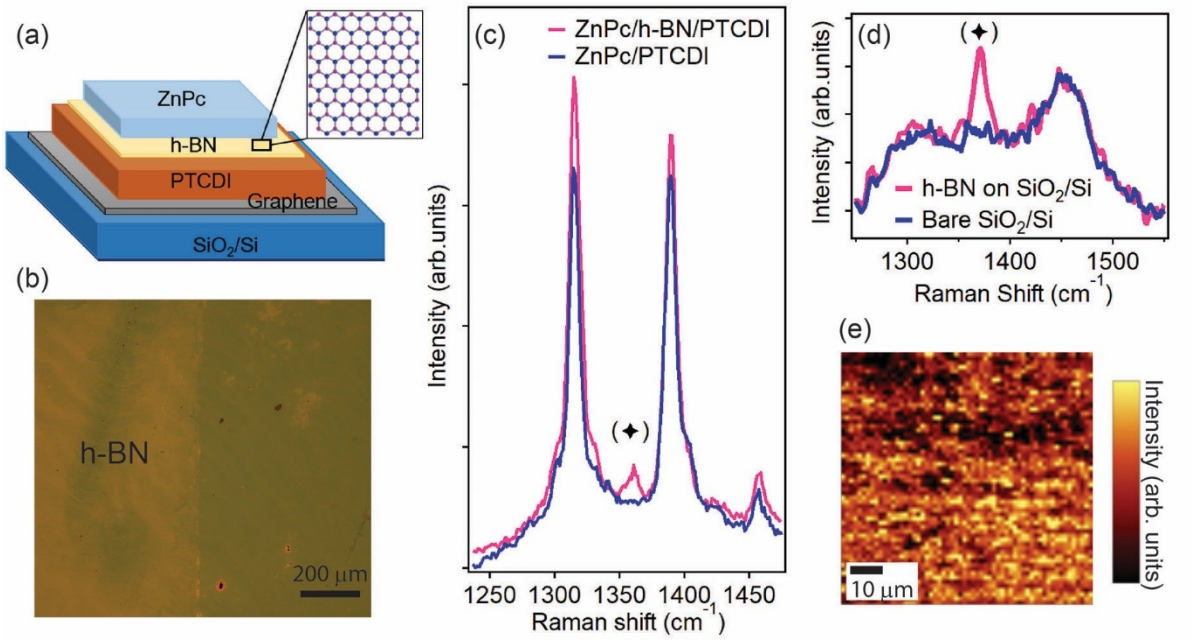

Figure 1. a) A schematic diagram shows how the h-BN film is sandwiched between donor and accepter layers deposited on graphene/SiO_2/Si. b) An optical microscope image of a 3-nm ZnPc/h-BN/5-nm PTCDI sample at the edge of the h-BN. c) The comparison of the Raman spectra of the 3-nm ZnPc/h-BN/5-nm PTCDI (red) and the 3-nm ZnPc/5-nm PTCDI samples (blue). The additional peak at ~1362 cm^{-1} is ascribed to the ML h-BN. d) The comparison of the Raman spectra of h-BN transferred on a SiO_2/Si substrate with the bare SiO_2/Si substrate. e) A Raman mapping image of the intensity of the h-BN's E_{2g} phonon mode. The uniform intensity indicates that the h-BN is continuous.

We have also performed UPS measurements on the transferred h-BN. The UPS measurement was done by using the He-I emission line (21.22 eV) generated from a standard UV discharge lamp. Figure 2 shows the UPS spectrum of the transferred h-BN on PTCDI. The energy axis is referenced with respect to the Fermi level (E_f). The spectrum was taken at the Γ point. The σ and π bands of h-BN are clearly visble and their energy positions agree well with previous measurments on exfoliated h-BN [27]. Because UPS is an extremely surface sensitive technique, the result indicates that the h-BN surface does not have a significant amount of contamination. Zooming into the spectral region near the Fermi level (inset in Fig. 2), the

PTCDI's HOMO peak can be seen although its intensity is attenuated as compared to spectrum obtained from the bare PTCDI sample (yellow line). Because the h-BN is continuous, the apparance of the PTCDI's HOMO peak shows that the h-BN/PTCDI interface does not have a significant amount of contamination which would have blocked photoelectrons originated from the underlying PTCDI layer.

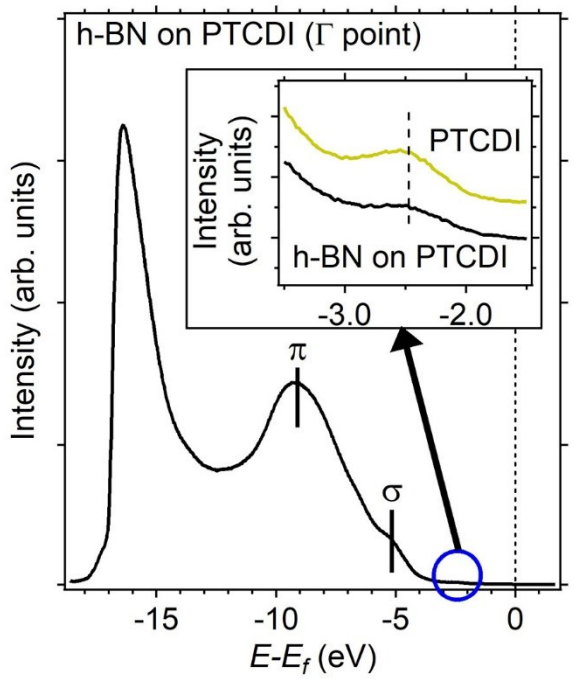

Figure 2. The UPS spectrum of the h-BN on 10-nm PTCDI sample. The spectrum is taken at the Γ point. The σ and π bands of h-BN are labelled. The region near the Fermi level is magnified and shown in the inset. In the inset, the spectrum is compared with the spectrum taken from a bare 10-nm PTCDI sample. The PTCDI's HOMO is visible in the h-BN on PTCDI spectrum.

We further measure the energy level alignment at the D-A interface with UPS. Figures 3a and 3b show the UPS spectra obtained from 10-nm PTCDI; 1-nm ZnPc/h-BN/10-nm PTCDI; and 10-nm ZnPc/h-BN/10-nm PTCDI samples. We also obtain UPS spectra for ZnPc/PTCDI samples without the h-BN interlayer, which are shown as blue lines in Fig. 3. The secondary electron cut-off (SECO) region of the UPS spectra is shown in Fig. 3a, while the region near the highest occupied molecular orbital (HOMO) peak is shown in Fig. 3b. The HOMO onsets of PTCDI and ZnPc are indicated by vertical lines in Fig. 3b, which can then be

used to determine the HOMO alignment. The energy level diagram for between the PTCDI and ZnPc is shown in Fig. 3c. The energy axis is referenced with respect to the Fermi level (E_f). The lowest unoccupied molecular orbital (LUMO) position in Fig. 3c is determined by using the reported HOMO-LUMO gaps (offset-to-offset) of the two molecules [28,29]. For the ZnPc, the HOMO offsets determined from those 1-nm samples are used to produce Fig. 3c, and the red and blue lines represent the energy level with and without h-BN interlayer, respectively. In both cases (with and without h-BN), the ZnPc/PTCDI has a type II band alignment, and the HOMO offset is not significantly affected by the insertion of the h-BN layer.

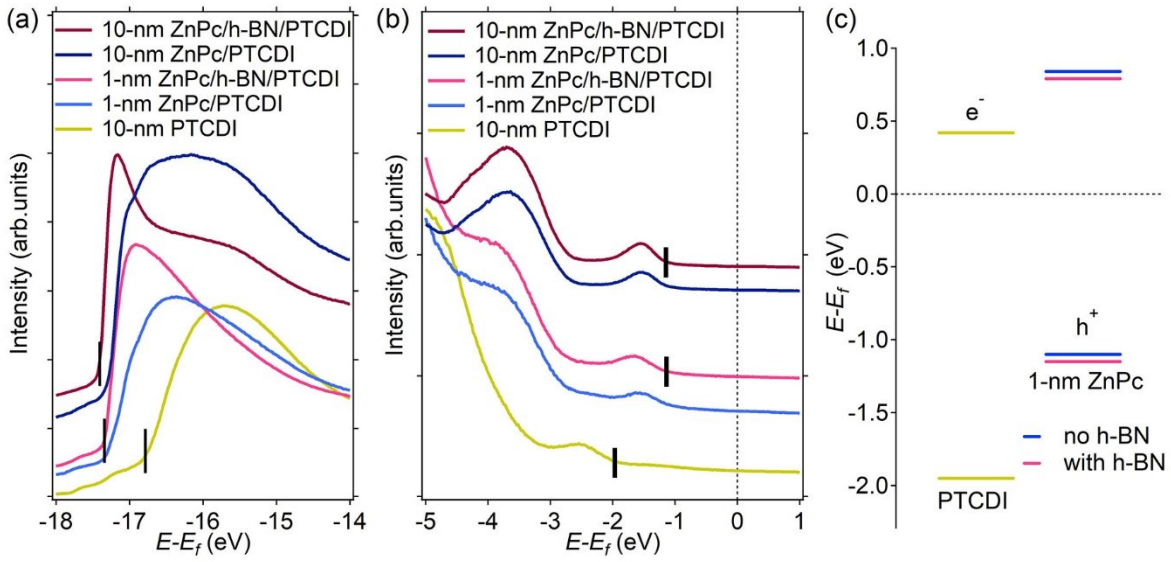

Figure 3. The UPS spectra of a series of samples with different thicknesses that are used to determine the HOMO level alignment at the ZnPc/h-BN/PTCDI interface. The samples used have the following thicknesses: 10-nm PTCDI; 1-nm ZnPc/h-BN/10-nm PTCDI, and 10-nm ZnPc/h-BN/10-nm PTCDI. The two blue lines represent spectra from ZnPc/PTCDI bilayer samples without the h-BN layer. The spectral regions a) near the SECO, and b) near the HOMO peak are shown. c) The band alignment of ZnPc/PTCDI determined from the UPS spectra. The red and blue lines represent the ZnPc's energy levels at interfaces with and without the h-BN, respectively. The LUMO levels were estimated using the HOMO-LUMO gap for the two molecules reported in Ref. [28,29].

The ionization potential (IP) of planar molecules such as ZnPc depends on the molecule's orientation with respect to the substrate [30-32]. We can use the IP value to determine whether the h-BN would have changed the orientation of the ZnPc molecule. For ZnPc and similar phthalocyanine molecules, multiple studies have shown that films with face-

on oriented molecules typically have an IP ~ 0.5 eV larger than that for films with edge-on oriented molecules [30-32]. The IP can be determined from the energy separation between SECO and HOMO onset. For the 10-nm PTCDI/graphene, the IP is 6.39 eV, which agrees well with the reported value for the face-on orientated PTCDI (6.42 eV [28]). The IP for the ZnPc, determined from samples with a 1-nm ZnPc top layer, is 5.03 eV and 5.01 eV for samples with and without h-BN, respectively. The two IPs are similar, which indicates that ZnPc molecules grown on h-BN and on PTCDI have a similar orientation. The IP for face-on oriented ZnPc is ~ 5.1 - 5.3 eV [25,29,30]. Hence, ZnPc has a primarily face-on orientation, but the slight decrease in the IP could be originated from a slight tilting of the ZnPc molecule with respect to the substrate. Previous works also show that phthalocyanine molecules grown on h-BN have a face-on orientation [33,34]. Because D-A interfaces with and without the h-BN have a similar energy level alignment and molecular orientation, a direct comparison between samples with and without the h-BN interlayer can be done to determine the effect of h-BN on CT and CS processes.

B. Impact of the h-BN on the charge transfer (CT) rate at the D-A interface

The h-BN interlayer can affect both the CT rate across the D-A interface, and the dissociation yield of the CT exciton (i.e. the CS yield). First, we used TR-TPPE to determine the initial electron transfer rate from ZnPc (donor) to PTCDI (acceptor). In this experiment, a 1.77 eV (700 nm) pump beam was used to selectively excite the singlet (S_1) exciton in the top ZnPc layer. Then, a time-delayed 4.59 eV (270 nm) probe beam was used to ionize the excited electron from ZnPc's S_1 exciton. Samples with different ZnPc thicknesses, and with or without h-BN were used. All samples have a 10 nm PTCDI bottom layer that was grown on graphene. The TPPE spectra near time-zero for different samples are shown in Fig. 4a. The final state energy of the electron with respect to the E_f is used for the energy axis. Subtracting the probe photon energy (4.59 eV) from the final state energy gives the energy of the excited state (known

as the intermediate state energy). As discussed in the supplemental material,[35] referencing the intermediate state energy with respect to the ZnPc's HOMO peak energy measured by UPS can give us the transition energy of the exciton. Such a plot is shown as Fig. S1 in the supplemental material.[35] In Fig. S1, the peak is located at 1.6 – 1.7 eV, which can be assigned to the ZnPc's S_1 exciton [36,37]. We note that similar approaches have been used by others to determine the exciton transition energy from the time-resolved photoemission spectrum [38].

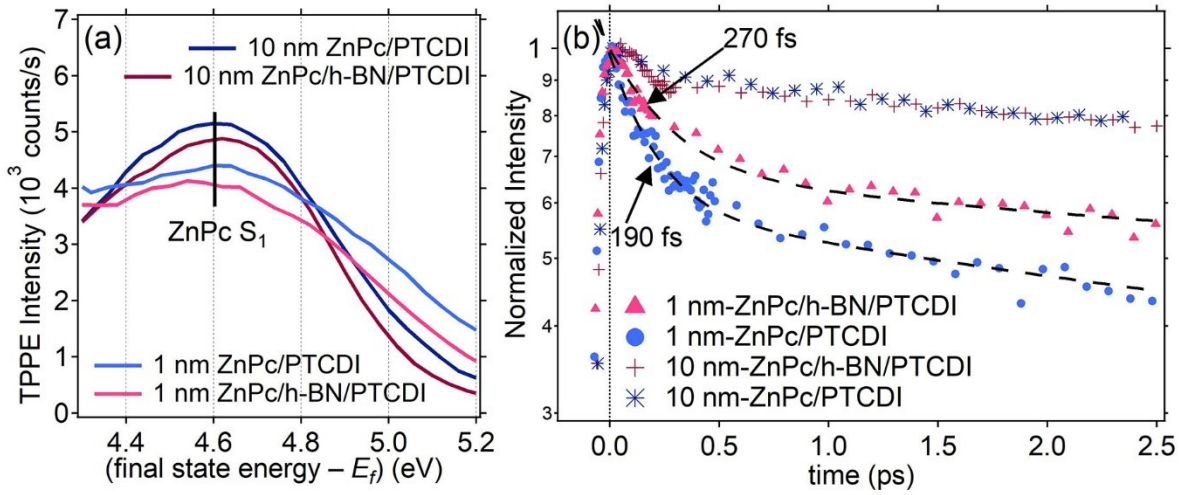

Figure 4. a) The TPPE spectra for different samples near the time zero. Based on our previous works, the peak at ~ 1.6 eV can be assigned to ZnPc's S_1. b) The integrated intensity of the ZnPc's S_1 peak as a function of time. The intensity near time-zero is normalized to 1. For the two samples with a 1-nm ZnPc layer, the initial rapid intensity decay is resulted from the CT from ZnPc to PTCDI.

Before discussing the time-resolved measurements, we note that the photoemission is a surface sensitive process. The electron inelastic mean free path (imfp) depends on the energy of the emitted electron and the nature of the material. Using the universal curve for organic compounds reported in Ref. [39], the final state energy on Fig. 4a, and a mass density of 1.7 g cm^{-3}, we found that the imfp is ~ 1.6 nm. A more recent work on pi-conjugated organic semiconductors shows that the imfp at an energy ~ 5 eV above E_f is ~ 3 nm [40]. Our previous study on ZnPc deposited on Au shows that when the ZnPc's thickness is larger than 4 nm, the sub-ps dynamics does not change with the film thickness, i.e. the photoemission probe is not

sensitive to the CT process at the buried interface for ZnPc films thicker than 4 nm [37]. Our previous measurement [37] implies that the imfp in our ZnPc films should be less than 4 nm, which is consistent with the reported imfp for organic materials [39,40]. Hence, in our case, the TPPE probes the ZnPc's S_1 exciton locating near the surface. We would like to stress that the imfp is highly depending on the material system. For inorganic materials, the imfp at low energies can reach up to ~ 10 nm [39].

Figure 4b shows the normalized intensity of the ZnPc's S_1 peak as a function of time. Results obtained from the two samples with a 1-nm ZnPc layer show a rapid intensity decay in the first few hundreds of femtoseconds (fs). For these samples, the S_1 exciton's delocalization size is larger than the ZnPc film thickness [37] and electron from the S_1 exciton can transfer directly (without the need of slow exciton diffusion) to PTCDI. Hence, the initial rapid signal decay can be primarily attributed to the electron transfer from ZnPc to PTCDI, which quenches the signal from the ZnPc's S_1 exciton. For the two 10-nm ZnPc samples, S_1 excitons near the surface cannot diffuse to the ZnPc's bottom interface immediately (< 1 ps) after photoexcitation [36]. Indeed, for the two 10-nm thick samples, the intensity decay does not depend on the underlying layers (Fig. 4b). In the supplemental material (Fig. S2) [35], we further compare the dynamics of five different 10-nm ZnPc samples deposited on different substrates. The same sub-ps decay dynamics is observed and is highly reproducible. Hence, we attribute the sub-ps intensity decay of those 10-nm samples to the intrinsic S_1 property of ZnPc, which can be originated from processes such as exciton localization or hot exciton relaxation [37]. For 1-nm samples, the small intrinsic intensity decay from ZnPc convolutes with the population quenching originated from the CT to produce the overall intensity decay. Hence, the convoluted intensity decay rate can systematically overestimate the actual CT rate. However, the extent of this overestimation should be small because the intensity decay originated from CT is much more pronounced than the intensity decay originated from the intrinsic S_1 dynamics.

The dynamics for the two 1 nm samples was fit with a biexponential decay function (dashed lines). The 1-nm ZnPc/PTCDI sample shows an initial decay time of 190 fs, which is faster than the decay time observed for the 1-nm ZnPc/h-BN/PTCDI sample (270 fs). We note that the decay rates obtained from the TR-TPPE experiments are highly reproducible and do not have much sample-to-sample variation. A comparison between data taken from different samples (but with the same thickness) are shown in Fig. S3 in the supplemental material.[35] When h-BN is inserted between the donor and the acceptor, the CT from ZnPc to PTCDI becomes slower. The h-BN layer spatially separates ZnPc and PTCDI, which reduces the overlapping between the two LUMO wave functions, and hence the CT rate. However, we note that the h-BN is thin enough (~ 0.3 nm) so that the CT from ZnPc to PTCDI can still occur at a reasonably fast rate (< 1 ps).

C. Impact of the h-BN on the photon-to-free carrier conversion yield

The interfacial CT process mentioned in the last section can produce CT excitons at the D-A interface [1-5]. However, these CT excitons are typically bound. To generate free carriers, these CT excitons must undergo successful CS before they recombine. To determine the photon-to-free carrier conversion yield, we utilize the graphene underlying our samples to probe the number of free charges generated from the CS process. Because the graphene's conductivity is highly sensitive to the charge doping, the number of separated charges injected into graphene can be quantified by measuring the resistance of the graphene layer R_G as a function of time. The ZnPc-PTCDI heterostructures, with and without the h-BN interlayer, were fabricated on GFET devices. During the measurement, the top ZnPc layer was selectively excited by 700-nm, 25-fs laser pulses. For a successful CS event, an electron injects into the graphene and the hole remains in the top ZnPc layer. The electron injection creates n-doping in graphene, which produces a measurable change in the R_G. The change in the graphene's channel resistance ($\Delta R_G/R_G$) was captured by a 200 MHz oscilloscope, which is proportional

to the number of separated charges after the pulse-laser excitation. We have previously developed this TR-GFET method to probe both the charge generation dynamics and the charge generation yield on organic D-A bilayer [23,41] and trilayer [24], and halide perovskite bulk heterostructures [42]. The detailed principle of our method can be found in Ref. [23].

Figures 5a and 5b show the time-resolved $\Delta R_G/R_G$ signal of a pair of samples, 3-nm ZnPc/h-BN/5-nm PTCDI and 3-nm ZnPc/5-nm PTCDI, on two different timescales. To compare the dynamics, the signal near time zero is normalized to 1. The separation of CT excitons produces free charges within the first few ns, which results in the rapid signal rise observed in Fig. 5a. The instrumental response time of our oscilloscope is ~ 2 ns, which is shown as the dashed line. The signal decay on longer timescales is shown in Fig. 5b, which represents the recombination of separated electron-hole pairs. The recombination time is long because the electron (residing in graphene) and the hole (residing in ZnPc) are separated by the 5 nm PTCDI layer. We note that the sample with the h-BN layer shows a somewhat slower recombination kinetics as compared to the sample without the h-BN layer. This behavior is expected because the h-BN layer spatially separates the PTCDI and ZnPc, which reduces the electron-hole recombination rate.

While it is important that the h-BN can reduce the recombination of electrons and holes that have already separated, our major goal is to determine whether the h-BN would enhance the CS yield of the CT exciton. The h-BN can increase the CS yield by three ways. First, it increases the average distance between the electron and hole in the CT exciton, which in turn reduces the CT exciton binding energy. Loosely bound CT excitons should have a faster CS rate because of the lower energy barrier for CS. Second, the h-BN has a slightly larger dielectric constant (~ 6.8, Ref. [43]) than organic materials, and it is known that h-BN can screen free charges from the substrate [44]. A better electronic screening from the environment can lower the exciton binding energy as well [45]. Third, the h-BN layer reduces the CT exciton

recombination rate by reducing the spatial overlap of the electron and hole wave functions. As a result of these two contributions, CT excitons have more time to undergo CS before it recombines. Therefore, the CS yield would be increased by the h-BN layer.

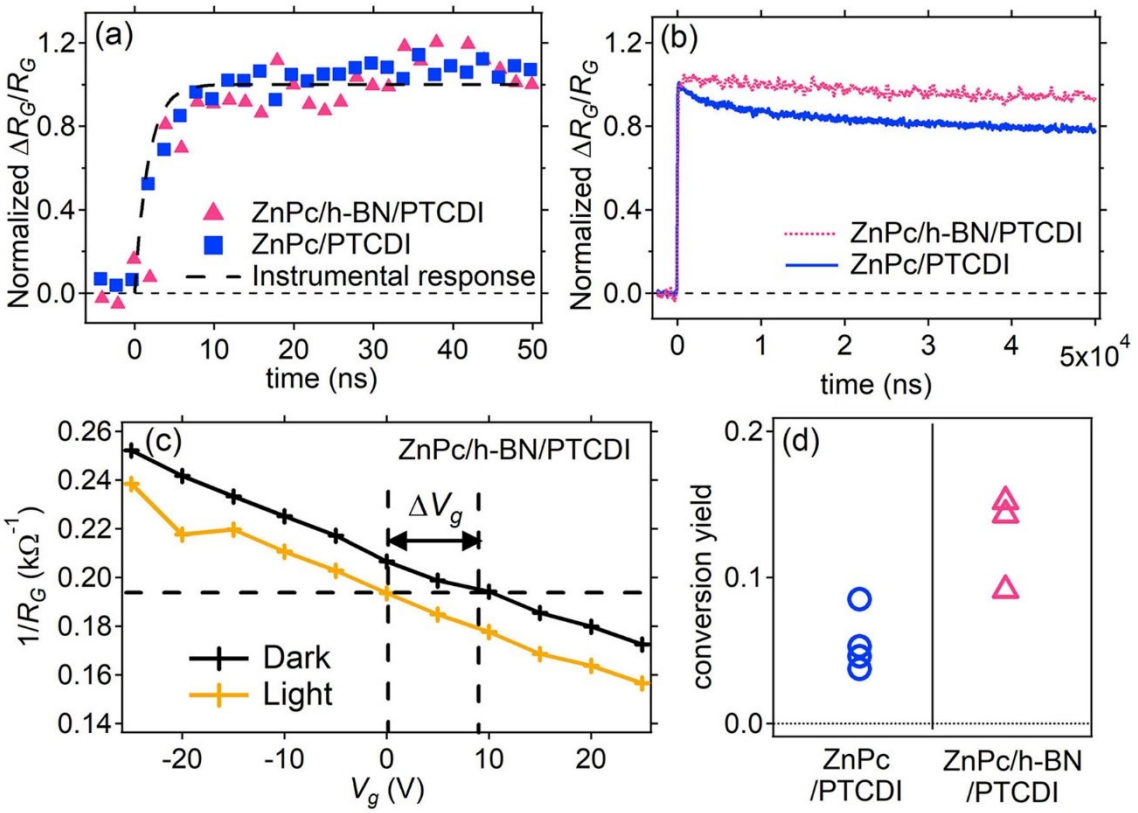

Figure 5. a, b) The normalized $\Delta R_G/R_G$ signal for ZnPc/h-BN/PTCDI (red) and ZnPc/PTCDI (blue) samples on the ns and μs timescales. For both samples, the thicknesses for ZnPc and PTCDI are 3 nm and 5 nm, respectively. c) The graphene's channel conductance ($1/R_G$) as a function of the gate voltage V_g for the 3-nm ZnPc/h-BN/5-nm PTCDI sample. The "dark" and "light" curves represent conductance before and ~ 10 ns after the arrival of the fs-pulse laser pulse. The horizontal shift of the curve (ΔV_g) can be used to calculate the number of separated charges. d) The calculated photon-to-free carrier conversion yield for several independent ZnPc/h-BN/PTCDI (red) and ZnPc/PTCDI (blue) samples.

The TR-GFET experiment was used to measure the photon-to-free carrier conversion yield, i.e. the number of free charges generated from the heterostructure per absorbed photons. An increase in the photon-to-free carrier conversion yield can be attributed to an increase in the CS yield. To measure the conversion yield, we use the resistance change (ΔR_G) at $t \approx 10$ ns to determine the number of separated carriers per unit area right after the initial CS process. In order to correlate ΔR_G with the actual number of separated carriers, back-gated samples with

the graphene transferred on SiO_2 (300 nm)/Si substrates were used. By applying a back gate voltage (V_g) to the SiO_2/Si back gate, the graphene can be doped electrically and the graphene's resistance as a function of V_g can be obtained. Because the number of carriers induced by the electrical gating can be determined simply by using the equation of a parallel plate capacitor, the V_g dependent measurement can be used to calibrate the response of each individual graphene sensor. A detailed description of this method can be found in our previous work [23]. At each gate voltage, the graphene's resistance was determined before (t < 0 ns), and immediately after the fs laser pulse excites the sample ($t \approx 10$ ns) by using time-traces similar to the one shown in Fig. 4a. Then, the conductance ($1/R_G$) before (labeled as "dark") and after (labeled as "light") the arrival of the fs laser pulse is plotted as a function of V_g. Figure 4c shows an example of these V_G dependent curves for a 3-nm ZnPc/h-BN/5-nm PTCDI sample.

In Fig. 5c, it is apparent that the whole curve shifts to the left after the arrival of the fs laser pulse. The direction of the shift (to the left) indicates that the graphene is doped with additional electrons and holes are trapped in the semiconductor layer (ZnPc in our case) [46]. The number of the electrons N, transferred to graphene after the CS process, can be related to the voltage shift (ΔV_g) by the equation for a parallel plate capacitor [47,48]:

$$N = \Delta V_g \frac{\kappa \varepsilon_0 A}{d} \frac{1}{e}, \quad (1)$$

where κ and d are the dielectric constant and the thickness of SiO_2 respectively, ε_0 is the vacuum permittivity, A is the area of the graphene channel and e is the electron charge. For our samples, we used κ = 3.6, d = 300 nm and A = 1 mm^2. Then, the photon-to-free carrier conversion yield is defined as N divided by the number of absorbed photons. The number of absorbed photons can be estimated by a transfer-matrix model that accounts for the interference effect in the multilayer sample. The details of the transfer-matrix model are described in our previous publication [23,24] and the supplement material [35]. In this work, we added the ML h-BN layer into our model, and the dielectric constants for ML h-BN was obtained from Ref.

[43]. At 700 nm, most of the optical absorption occurs at the ZnPc layer. In order to provide a more accurate estimation of the optical absorption, we previously measured the optical extinction coefficient on a series of ZnPc films with different thicknesses [23].

Figure 5d shows the calculated conversion yield for samples with and without the h-BN layer. For all samples, the thicknesses of ZnPc and PTCDI are fixed at 3 nm and 5 nm, respectively. In our samples, because the graphene is not connected to the ZnPc layer through an external circuit, the separated charges are not extracted out from the sample. Hence, our samples are essentially at the open-circuit condition, which can explain the apparently low photon-to-free carrier conversion yield (< 20 %). The measured conversion yield represents how much separated charges can be produced transiently on ns timescales after the fs-laser pulse excitation. We note that the laser repetition rate was reduced to 100 Hz to ensure that all these separated charges recombine before the arrival of the next pulse. In Fig. 5d, each data point represents a measurement from an independent GFET device. We note that the GFET measurement probes the overall charge conversion yield, which can be sensitive to multiple electronic processes such as charge transport, trapping, and recombination. The rates of these processes are sensitive to the amount of imperfections in the sample. The device-to-device variations in the conversion yield can be originated from imperfections introduced during the graphene and h-BN transfer. Despite this variation, it is apparent that ZnPc/h-BN/PTCDI samples show a larger yield than ZnPc/PTCDI samples. The average conversion yield increases from ~ 5.5 % to ~ 12.9 % after the h-BN is added, which represents a 130% increase (i.e., the yield is more than doubled). Therefore, we can conclude that the h-BN improves the CS yield by suppressing the formation of tightly bound CT excitons and various recombination processes.

Finally, we note that the h-BN slows down all electron transfer processes between the donor and the acceptor. It may not be apparent that the enhancement in the CS yield can

outweigh the reduction in the initial CT rate, which leads to an overall improvement in the photon-to-free carrier conversion yield. We argue that the initial CT process often involves delocalized states with excess energies [3,7,49,50]. Compared to recombination processes initiated by cold and localized states, the delocalized nature of these hot states would make the initial CT process less susceptible to the increase in the distance between donor and acceptor molecules. Hence, the atomically thin h-BN layer should have a lesser impact on the initial CT rate than on recombination rates. Moreover, the initial CT process at the D-A interface is very fast (~ 100 fs) as compared to other competing electronic processes. Hence, a slower CT process would not be detrimental in decreasing the yield for forming CT excitons. By contrast, for the CS process, the h-BN not only decreases the CT exciton recombination rate, but it also increases the CS rate by lowering the exciton binding energy. Both effects can increase the CS yield. According to this understanding, the overall photon-to-free carrier conversion yield would be further boosted by using two or more h-BN layers. However, the yield will decrease drastically when the h-BN layer is thick enough to block the initial CT process. The strategy discussed here should also be applicable to other organic D-A interfaces.

IV. CONCLUSION

In this work, we have demonstrated the use of ML h-BN as an ultrathin insulating barrier for enhancing the CS yield of CT excitons at an organic D-A interface. Compared to its counterpart of conventional thin film insulating materials that have been previously used, the ML h-BN has advantages of atomically small thickness of 0.33 nm, negligible mixing at the D-A interface, and continuity over a macroscopic area (on the order of cm^2). Hence, it can effectively block the formation of tightly bound-CT excitons and reduce the recombination of electron-hole pairs across the whole macroscopic interface. The small thickness of the ML h-BN means that it does not significantly reduce the interfacial CT rate. Specifically, we found that although the ML h-BN slows the electron transfer from ZnPc to PTCDI (the CT time

increases from 190 fs to 270 fs), it increases the photon-to-free carrier conversion yield from ~5.5% to ~12.9%. In our experiment, the conversion yield was measured in a condition similar to the open circuit condition found in PV devices. The enhanced yield at this zero-field condition implies that a smaller internal E-field, and hence a smaller voltage loss, would be needed for producing the photocurrent. Together with the reduction in electron-hole recombination, the ML h-BN can potentially increase the open circuit voltage and the fill factor if it is incorporated at the D-A interface in ultrathin bilayer or multilayer OPV devices.

ACKNOWLEDGEMENT

This work was supported by US National Science Foundation grants DMR-2109979. The support by the University of Kansas General Research Fund allocation #2151080 is also acknowledged. J. Z. W. acknowledges US National Science Foundation grants NSF-ECCS-1809293 and NSF-DMR-1909292, and US Army grant W909MY-21-C-0033. F.R. acknowledges the scholarship support from Jazan University.

REFERENCES

[1] J. L. Bredas, J. E. Norton, J. Cornil, and V. Coropceanu, Molecular Understanding of Organic Solar Cells: The Challenges, Acc. Chem. Res. **42**, 1691 (2009).

[2] T. M. Clarke and J. R. Durrant, Charge Photogeneration in Organic Solar Cells, Chem. Rev. **110**, 6736 (2010).

[3] A. J. Heeger, 25th Anniversary Article: Bulk Heterojunction Solar Cells: Understanding the Mechanism of Operation, Adv. Mater. **26**, 10 (2014).

[4] O. Ostroverkhova, Organic Optoelectronic Materials: Mechanisms and Applications, Chem. Rev. **116**, 13279 (2016).

[5] C. S. Ponseca, P. Chabera, J. Uhlig, P. Persson, and V. Sundstrom, Ultrafast Electron Dynamics in Solar Energy Conversion, Chem. Rev. **117**, 10940 (2017).

[6] X. Y. Zhu, Q. Yang, and M. Muntwiler, Charge-Transfer Excitons at Organic Semiconductor Surfaces and Interfaces, Acc. Chem. Res. **42**, 1779 (2009).

[7] T. Wang, T. R. Kafle, B. Kattel, and W.-L. Chan, A Multidimensional View of Charge Transfer Excitons at Organic Donor–Acceptor Interfaces, J. Am. Chem. Soc. **139**, 4098 (2017).

[8] J. Z. Yao, T. Kirchartz, M. S. Vezie, M. A. Faist, W. Gong, Z. C. He, H. B. Wu, J. Troughton, T. Watson, D. Bryant, and J. Nelson, Quantifying Losses in Open-Circuit Voltage in Solution-Processable Solar Cells, Phys. Rev. Appl. **4**, 014020 (2015).

[9] B. P. Rand, D. P. Burk, and S. R. Forrest, Offset energies at organic semiconductor heterojunctions and their influence on the open-circuit voltage of thin-film solar cells, Phys. Rev. B **75**, 115327 (2007).

[10] X. Liu, B. P. Rand, and S. R. Forrest, Engineering Charge-Transfer States for Efficient, Low-Energy-Loss Organic Photovoltaics, Trends in Chemistry **1**, 815 (2019).

[11] Y. F. Zhong, A. Tada, S. Izawa, K. Hashimoto, and K. Tajima, Enhancement of V-OC without Loss of J(SC) in Organic Solar Cells by Modification of Donor/Acceptor Interfaces, Adv Energy Mater **4** (2014).

[12] S. Sampat, A. D. Mohite, B. Crone, S. Tretiak, A. V. Malko, A. J. Taylor, and D. A. Yarotski, Tunable Charge Transfer Dynamics at Tetracene/LiF/C-60 Interfaces, J. Phys. Chem. C **119**, 1286 (2015).

[13] Y. L. Huang, Y. J. Zheng, Z. B. Song, D. Z. Chi, A. T. S. Wee, and S. Y. Quek, The organic-2D transition metal dichalcogenide heterointerface, Chem. Soc. Rev. **47**, 3241 (2018).

[14] H. M. Wang, C. H. Li, P. F. Fang, Z. L. Zhang, and J. Z. Zhang, Synthesis, properties, and optoelectronic applications of two-dimensional MoS2 and MoS2-based heterostructures, Chem. Soc. Rev. **47**, 6101 (2018).

[15] S. H. Amsterdam, T. J. Marks, and M. C. Hersam, Leveraging Molecular Properties to Tailor Mixed-Dimensional Heterostructures beyond Energy Level Alignment, J. Phys. Chem. Lett. **12**, 4543 (2021).

[16] M. Gobbi, E. Orgiu, and P. Samori, When 2D Materials Meet Molecules: Opportunities and Challenges of Hybrid Organic/Inorganic van der Waals Heterostructures, Adv. Mater. **30**, 1706103 (2018).

[17] L. Qin, B. Kattel, T. R. Kafle, M. Alamri, M. Gong, M. Panth, Y. Hou, J. Wu, and W. L. Chan, Scalable Graphene-on-Organometal Halide Perovskite Heterostructure Fabricated by Dry Transfer, Adv. Mater. Interfaces **6**, 1801419 (2019).

[18] K. L. Zhang, Y. L. Feng, F. Wang, Z. C. Yang, and J. Wang, Two dimensional hexagonal boron nitride (2D-hBN): synthesis, properties and applications, J. Mater. Chem. C **5**, 11992 (2017).

[19] K. Nakano and K. Tajima, Organic Planar Heterojunctions: From Models for Interfaces in Bulk Heterojunctions to High-Performance Solar Cells, Adv. Mater. **29** (2017).

[20] K. Cnops, B. P. Rand, D. Cheyns, B. Verreet, M. A. Empl, and P. Heremans, 8.4% efficient fullerene-free organic solar cells exploiting long-range exciton energy transfer, Nat. Commun. **5**, 3406 (2014).

[21] X. D. Chen, Z. B. Liu, C. Y. Zheng, F. Xing, X. Q. Yan, Y. S. Chen, and J. G. Tian, High-quality and efficient transfer of large-area graphene films onto different substrates, Carbon **56**, 271 (2013).

[22] X. S. Li, Y. W. Zhu, W. W. Cai, M. Borysiak, B. Y. Han, D. Chen, R. D. Piner, L. Colombo, and R. S. Ruoff, Transfer of Large-Area Graphene Films for High-Performance Transparent Conductive Electrodes, Nano Lett. **9**, 4359 (2009).

[23] B. Kattel, L. Qin, T. R. Kafle, and W. L. Chan, Graphene Field-Effect Transistor as a High-Throughput Platform to Probe Charge Separation at Donor-Acceptor Interfaces, J. Phys. Chem. Lett. **9**, 1633 (2018).

[24] S. Wanigasekara, B. Kattel, F. Rudayni, and W. L. Chan, Extracting Electrons from Delocalized Excitons by Flattening the Energetic Pathway for Charge Separation, J. Phys. Chem. Lett. **12**, 9047 (2021).

[25] T. Wang, T. R. Kafle, B. Kattel, Q. F. Liu, J. Wu, and W. L. Chan, Growing Ultra-flat Organic Films on Graphene with a Face-on Stacking via Moderate Molecule-Substrate Interaction, Sci. Rep. **6**, 28895 (2016).

[26] R. V. Gorbachev, I. Riaz, R. R. Nair, R. Jalil, L. Britnell, B. D. Belle, E. W. Hill, K. S. Novoselov, K. Watanabe, T. Taniguchi, A. K. Geim, and P. Blake, Hunting for Monolayer Boron Nitride: Optical and Raman Signatures, Small **7**, 465 (2011).

[27] R. J. Koch, J. Katoch, S. Moser, D. Schwarz, R. K. Kawakami, A. Bostwick, E. Rotenberg, C. Jozwiak, and S. Ulstrup, Electronic structure of exfoliated and epitaxial hexagonal boron nitride, Phys Rev Mater **2**, 074006 (2018).

[28] D. R. T. Zahn, G. N. Gavrila, and M. Gorgoi, The transport gap of organic semiconductors studied using the combination of direct and inverse photoemission, Chem. Phys. **325**, 99 (2006).

[29] W. Y. Gao and A. Kahn, Electronic structure and current injection in zinc phthalocyanine doped with tetrafluorotetracyanoquinodimethane: Interface versus bulk effects, Org. Electron. **3**, 53 (2002).

[30] W. Chen, H. Huang, S. Chen, Y. L. Huang, X. Y. Gao, and A. T. S. Wee, Molecular Orientation-Dependent Ionization Potential of Organic Thin Films, Chem. Mater. **20**, 7017 (2008).

[31] S. Duhm, G. Heimel, I. Salzmann, H. Glowatzki, R. L. Johnson, A. Vollmer, J. P. Rabe, and N. Koch, Orientation-dependent ionization energies and interface dipoles in ordered molecular assemblies, Nat. Mater. **7**, 326 (2008).

[32] M. Schwarze, K. S. Schellhammer, K. Ortstein, J. Benduhn, C. Gaul, A. Hinderhofer, L. P. Toro, R. Scholz, J. Kublitski, S. Roland, M. Lau, C. Poelking, D. Andrienko, G. Cuniberti, F. Schreiber, D. Neher, K. Vandewal, F. Ortmann, and K. Leo, Impact of molecular quadrupole moments on the energy levels at organic heterojunctions, Nat. Commun. **10**, 2466 (2019).

[33] M. Iannuzzi, F. Tran, R. Widmer, T. Dienel, K. Radican, Y. Ding, J. R. Hutter, and O. Groning, Site-selective adsorption of phthalocyanine on h-BN/Rh(111) nanomesh, PCCP **16**, 12374 (2014).

[34] F. Schulz, R. Drost, S. K. Hamalainen, and P. Liljeroth, Templated Self-Assembly and Local Doping of Molecules on Epitaxial Hexagonal Boron Nitride, ACS Nano **7**, 11121 (2013).

[35] See Supplemental Material at [URL will be inserted by publisher] for the supporting data.

[36] T. Wang, Q. F. Liu, C. Caraiani, Y. P. Zhang, J. Wu, and W. L. Chan, Effect of Interlayer Coupling on Ultrafast Charge Transfer from Semiconducting Molecules to Mono- and Bilayer Graphene, Phys. Rev. Appl. **4**, 014016 (2015).

[37] T. Wang and W. L. Chan, Dynamical Localization Limiting the Coherent Transport Range of Excitons in Organic Crystals, J. Phys. Chem. Lett. **5**, 1812 (2014).

[38] M. K. L. Man, J. Madeo, C. Sahoo, K. C. Xie, M. Campbell, V. Pareek, A. Karmakar, E. L. Wong, A. Al-Mahboob, N. S. Chan, D. R. Bacon, X. Zhu, M. M. M. Abdelrasoul, X. Q. Li, T. F. Heinz, F. H. da Jornada, T. Cao, and K. M. Dani, Experimental measurement of the intrinsic excitonic wave function, Sci. Adv. **7**, eabg0192 (2021).

[39] M. P. Seah and W. A. Dench, Quantitative Electron Spectroscopy of Surfaces: A Standard Data Base foe Electron Inelastic Mean Free Paths in Solids, Surf. Interface Anal. **1**, 2 (1979).

[40] Y. Ozawa, Y. Nakayama, S. Machida, H. Kinjo, and H. Ishii, Maximum probing depth of low-energy photoelectrons in an amorphous organic semiconductor film, J. Electron. Spectrosc. Relat. Phenom. **197**, 17 (2014).

[41] T. R. Kafle, B. Kattel, T. Wang, and W.-L. Chan, The relationship between the coherent size, binding energy and dissociation dynamics of charge transfer excitons at organic interfaces, J. Phys.: Condens. Matter **30**, 454001 (2018).

[42] L. Qin, L. P. Wu, B. Kattel, C. H. Li, Y. Zhang, Y. B. Hou, J. Wu, and W. L. Chan, Using Bulk Heterojunctions and Selective Electron Trapping to Enhance the Responsivity of Perovskite-Graphene Photodetectors, Adv. Funct. Mater. **27**, 1704173 (2017).

[43] A. Laturia, M. L. Van de Put, and W. G. Vandenberghe, Dielectric properties of hexagonal boron nitride and transition metal dichalcogenides: from monolayer to bulk, npj 2D Materials and Applications **2**, 6 (2018).

[44] K. Noori, N. L. Q. Cheng, F. Y. Xuan, and S. Y. Quek, Dielectric screening by 2D substrates, 2D Mater. **6**, 035036 (2019).

[45] A. Raja, A. Chaves, J. Yu, G. Arefe, H. M. Hill, A. F. Rigosi, T. C. Berkelbach, P. Nagler, C. Schuller, T. Korn, C. Nuckolls, J. Hone, L. E. Brus, T. F. Heinz, D. R. Reichman, and A. Chernikov, Coulomb engineering of the bandgap and excitons in two-dimensional materials, Nat. Commun. **8**, 15251 (2017).

[46] G. Konstantatos, M. Badioli, L. Gaudreau, J. Osmond, M. Bernechea, F. P. G. de Arquer, F. Gatti, and F. H. L. Koppens, Hybrid graphene-quantum dot phototransistors with ultrahigh gain, Nat. Nanotechnol. **7**, 363 (2012).

[47] Y. B. Zhang, T. T. Tang, C. Girit, Z. Hao, M. C. Martin, A. Zettl, M. F. Crommie, Y. R. Shen, and F. Wang, Direct observation of a widely tunable bandgap in bilayer graphene, Nature **459**, 820 (2009).

[48] J. B. Oostinga, H. B. Heersche, X. L. Liu, A. F. Morpurgo, and L. M. K. Vandersypen, Gate-induced insulating state in bilayer graphene devices, Nat. Mater. **7**, 151 (2008).

[49] S. M. Falke, C. A. Rozzi, D. Brida, M. Maiuri, M. Amato, E. Sommer, A. De Sio, A. Rubio, G. Cerullo, E. Molinari, and C. Lienau, Coherent ultrafast charge transfer in an organic photovoltaic blend, Science **344**, 1001 (2014).

[50] A. A. Bakulin, A. Rao, V. G. Pavelyev, P. H. M. van Loosdrecht, M. S. Pshenichnikov, D. Niedzialek, J. Cornil, D. Beljonne, and R. H. Friend, The Role of Driving Energy and Delocalized States for Charge Separation in Organic Semiconductors, Science **335**, 1340 (2012).

[51] C. C. Katsidis and D. I. Siapkas, General transfer-matrix method for optical multilayer systems with coherent, partially coherent, and incoherent interference, Appl. Opt. **41**, 3978 (2002).

[52] B. Harbecke, Coherent and Incoherent Reflection and Transmission of Multilayer Structures, Appl. Phys. B-Photo **39**, 165 (1986).

[53] S. J. Byrnes, Multilayer optical calculations, arXiv:1603.02720v2 (2016).

[54] M. Friedrich, T. Wagner, G. Salvan, S. Park, T. U. Kampen, and D. R. T. Zahn, Optical constants of 3,4,9,10-perylenetetracarboxylic dianhydride films on silicon and gallium arsenide studied by spectroscopic ellipsometry, Appl. Phys. A-Mater. **75**, 501 (2002).

[55] S. Cheon, K. D. Kihm, H. G. Kim, G. Lim, J. S. Park, and J. S. Lee, How to Reliably Determine the Complex Refractive Index (RI) of Graphene by Using Two Independent Measurement Constraints, Sci. Rep. **4**, 6364 (2014).

[56] H. J. Lee, C. H. Henry, K. J. Orlowsky, R. F. Kazarinov, and T. Y. Kometani, Refractive-Index Dispersion of Phosphosilicate Glass, Thermal Oxide, and Silicon-Nitride Films on Silicon, Appl. Opt. **27**, 4104 (1988).

[57] D. E. Aspnes and A. A. Studna, Dielectric Functions and Optical-Parameters of Si, Ge, GaP, GaAs, GaSb, InP, InAs, and InSb from 1.5 to 6.0 eV, Phys. Rev. B **27**, 985 (1983).